Fabrication of Tissue-Mimetic Environments Using Projection Stereolithography

by

Hang Yin

B.S., Beihang University, 2014

A thesis submitted to the

Faculty of the Graduate School of the

University of Colorado in partial fulfillment

of the requirement for the degree of

Master of Science

Department of Mechanical Engineering

2017

This thesis entitled:
Fabrication of Tissue-Mimetic Environments Using Projection Stereolithography
written by Hang Yin
has been approved for the Department of Mechanical Engineering

Prof. Xiaobo Yin

Prof. Wei Tan

Prof. Yifu Ding

Date

The final copy of this thesis has been examined by the signatories, and we find that both the content and the form meet acceptable presentation standards of scholarly work in the above mentioned discipline.

Abstract

Hang Yin (M.S., Mechanical Engineering)

Fabrication of tissue-mimetic environments using projection stereolithography

Thesis directed by Prof. Xiaobo Yin & Prof. Wei Tan

The stiffness of an extracellular matrix (ECM) can exert great influence on cellular functions such as proliferation, migration and differentiation. Challenges still remain, however, in the fabrication of artificial ECMs with well-controlled stiffness profiles in three dimension (3D). In this thesis, we developed a projection micro-stereolithography system to fabricate 3D structures with quantitative control over stiffness using biocompatible materials. The technique is based on a grayscale printing method, which spatially controls the crosslinking density in the 3D hydrogel structures without influencing their appearance. Mimetic tissue environments in the form of 2D striped patterns and 3D tubes with stiffness gradients were fabricated. Finally, we seeded bovine pulmonary arterial smooth muscle cells on these engineered environments, and during the culturing, cells migrated to stiffer regions. This work provides a method for fabricating tissue mimetic environments that can benefit the study of cellular behavior and other biomedical research.

Acknowledgements

First, I would like to express my deep gratitude to my advisor, Professor Xiaobo Yin. He gave me a lot of inspiration for the research like drawing sketches on my blank paper of scientific thinking. Although I stumbled around many challenges, he always pointed me in the right direction and encouraged me along the way.

Also, I would like to thank my co-advisor, Professor Wei Tan. She taught me to always stay positive and I learned to find solutions even if the problem seemed like it could not be solved. This project could not have been completed without her great patience and kindest support.

I am very grateful to the people who helped me solve problems related to the experiments. Thanks to Prof. Yifu Ding for discussing the development of my experimental method; thanks to Dr. Yonghui Ding for his expertise on the seeding and culture of cells that made the study of effect of stiffness over cell organization possible; to Dr. Yaoguang Ma for his help teaching me how to use SEM properly to improve the quality of the images; to Sabrina for her help in discussion and developing experiments; and thanks to all my lab mates who broadened my mind and generously provided ideas.

I want to say thank you to my girlfriend, Yize Zang, for her love, understanding and encouragement. Thank you for making me a priority and for your willingness to always help me, whether in studying or in daily life and thank you for always giving me infinite hope.

I am deeply indebted to my parents since I cannot be with them during these years. Despite the distance, they always checked in on me from China and made sure I knew they loved me unconditionally. I want to dedicate this thesis work to them.

Contents

Tables

Figures

Chapter 1 Introduction

Three-dimensional (3D) printing, also known as additive manufacturing, benefits many areas such as engineering, art, consumer products and manufacturing [4]. 3D printing is also widely employed in tissue engineering through the combination of engineering methods, material science and biomedical technologies. Recent research has revealed that culturing cells in 3D provides a more physiologically relevant environment for observing real cell behavior compared to 2D culture systems [5, 6]. Considerable advances have been made in 3D microfabrication techniques to make functional 3D structures that can mimic natural matrices for culturing cells. However, the fabrication resolution and shape of the structure are not the only requirements for tissue engineering. In particular, the mechanical properties of the printed extracellular matrix (ECM) should also be considered because the position dependent stiffness affect the cell organizations and migrations [7, 8]. The ability of normal cells to migrate up the rigidity gradient towards greater stiffness is called durotaxis and has been well studied [9]. Therefore, fabricating 3D tissue mimetic environments with defined 3D stiffness profiles can help better understand the role of stiffness on cellular biomechanical behaviors.

There are two major types of 3D printing methods that allow fabricating 3D ECM structures with potentials of stiffness control. The first is the inkjet bioprinting method [10, 11]. The inject printing process usually extrudes and then stabilizes the bioink to maintain a printed structure. For instance, direct foam writing can construct cellular ceramic structures with tailored geometry and mechanical properties [12]. This is an important step in the scalable fabrication of porous materials with stiffness control for tissue scaffolds. Despite the advantages of simplicity, flexibility and low cost, the inkjet bioprinting technology has many limitations. First, the resolution

of the structure is limited by the size of the nozzle on the printer. Second, the printed structures are hard to maintain their shapes especially for photo-crosslinkable hydrogel materials. Third, the viscosity of the bioink often induces shear force during the printing process, which compromises the viability of cells.

The second method is light-based bioprinting. This method utilizes the photo-polymerizable biomaterials. By spatially and temporally controlling the dosage of light exposure, this method initiates a crosslinking of the material and forms solid polymer structures. There are mainly two kinds of light-assisted methods. The first is the projection-based method. People use either a Digital Micro-Mirror Device (DMD) or Liquid Crystal over Silicon (LcoS) chip to modulate Ultraviolet (UV) light, then project user-defined patterns into the solution for 2D exposure [13]. Repeating the 2D exposure process in a consecutive, and layer-by-layer manner allows efficient constructing of 3D structures. The method has been explored to control the stiffness of the polymerized structures. For example, the method created suspended cantilever with different flexural modulus [14]. It can also create 2D stiffness gradient through grayscale exposure [15]. Compared to the inkjet method, the DMD method usually has a higher spatial resolution, usually in micron scale. It is also more efficient because it can polymerize a layer at one time. However, support structures may be needed in the fabrication process for some complex 3D structures, and it is also difficult to remove these support structures. Although the chemical etching method can solve this problem, it is time consuming and not particularly efficient [16]. The other light-based 3D printing method uses tightly focused laser spot to crosslink photopolymers along a specific contour [17], and nonlinear optical processes such as two photon polymerizations were often used for its improved spatial resolution and 3D structure forming capability. Because the two-photon absorption only happens at the center of the focus region where the energy is above

the threshold for the nonlinear effect, it can provide sub-micron resolutions. For example, two-photon lithography has been used to degrade the crosslink for photo degradable biomaterials so that the region where the two-photon absorption happens will be softer [18]. The two-photon lithography can provide the highest resolution among all the methods introduced thus far. However, the efficiency is not high in making stiffness gradient structures since post treatment is needed for most of cases.

In this work, we used DMD-based projection stereolithography as the printing method for the following reasons: (1) The resolution of the method can reach micron scale that can fulfil the need to fabricate complex 3D ECMs. (2) The printing efficiency and stability is the highest among all printing methods at this scale. (3) Biocompatible materials have been performed successfully by using this method.

For the projection-based 3D printing method, many materials have been used for different purposes of application. HDDA is a UV-curable monomer based on acrylates which has been used to develop high-resolution, 3D micro electro-mechanical systems. It has been widely used because of its low viscosity and many kinds of photo initiators and UV absorbers have high solubility in its solution. C. Sun presented the development of a high-resolution projection stereolithography process and realized the smallest feature of 0.6 μm with HDDA [19]. Compared with HDDA structures, PEG-based oligomer is also UV curable and the cured hydrogel structures can have more easily tunable physical properties and provide better chemical compatibility to hold cells. For example, Y. Lu used poly (ethylene glycol) diacrylates as the material to fabricate 3D scaffold, and he successfully encapsulated and seeded murine bone marrow-derived cells on the scaffold [20]. In another study, W. Zhu dissolved different kinds of materials in PEG solution to fabricate different parts of a fish body and applied the multi-exposure method to show the potential

application of drug delivery [17]. Although PEG-based hydrogel has been extensively used in the biomedical field, the materials mixed in the PEG solution and concentrations can be different to fulfil different research needs. For example, by mixing nanoparticles into the PEGDA solution and using laser scanning can further induce the crosslinking density at hydrogel surface so that can control the stiffness at certain regions [19]. Cells have been seeded on these gradient stiffness areas and it is discovered that cells organized along the stiffer regions on the surface of the hydrogel. In another example, PEGDMA solutions with different molecular weight and concentrations were used to generate bulk hydrogel structures with different moduli and human bone marrow-derived mesenchymal stem cells (MSCs) were found to be predominately elongated at regions with low stiffness while remained contracted in a circle within the high stiffness volumes [21]. After considering the extensive body of research on PEG-based materials for biomedical applications, poly (ethylene glycol) dimethacrylates (PEGDMA 750 Da) was used in this work. Compared with most of PEGDMA materials, this one has a relatively lower molecular weight and can generate a smaller mesh size of crosslink to form a stiffer structure after polymerization. In this way, PEGDMA 750 Da can provide us with a large range of values for tuning the elasticity of the ECMs.

Although the projection stereolithography has been developed for decades, and PEG-based materials were largely used for fabricating ECMs, the study of overall control of stiffness for 3D ECMs is still rare. There are many challenges to realize the goal. At first, the development of the projection stereolithography system. The resolution of the system has to reach micron scale and has the capability of making 3D structures. Second, the quantitative control over the stiffness of structures has to be realized and characterized. Third, the seeding and culturing of cells over the fabricated ECMs has to be performed.

In order to solve these problems, the thesis is organized as follows:

Chapter 1 provides an overview of 3D printing method to fabricate structures for biomedical application. It then introduces the materials used for projection stereolithography and is followed by the organization of the thesis work.

Chapter 2 describes the design of the 3D printing system, including optics design, motion design and prepolymer solution substrate design.

Chapter 3 introduces the materials used for the experiments and develops a simplified model to simulate the curing depth of printing. The whole process of the free radical polymerization is explained with the effect of oxygen inhibition reaction.

Chapter 4 illustrates the characterization of the projection stereolithography system. The roles of the components in the materials is demonstrated, and the printing process with 3D structures are described.

Chapter 5 demonstrates the fabrication of 3D structures with stiffness control using grayscale method. Atomic Force Microscope was used to quantify the elasticity of multilayer structures and the qualitative effect of stiffness over 3D structures is described using the buckling phenomenon of standing rods. Then bovine pulmonary arterial smooth muscle cells were seeded on the 3D printed structures to show the phenomenon of organization preference.

Chapter 2 System Design of Projection Stereolithography

2.1 Introduction

The projection stereolithography was first introduced by Takagi et al., in 1993 [22]. They used a solid mask to project patterns onto the liquid resin surface for fabrication. People keep using this method until now because it is very straightforward and the mask can be easily stored and reused. However, it is time-consuming to make so many physical masks to fit various kinds of need. Moreover, if the requirement for the design and manufacture of the mask is too large, it will lead to a huge amount of cost. In order to solve this problem, in 1997 Bertsch et al. demonstrated a method to generate a dynamic mask using Liquid Crystal Display (LCD) panel to display different patterns for projection micro stereolithography [23]. The dynamic mask changes the appearance of the mask by simply changing the patterns shown on the mask. This is a more efficient method compared to the traditional way and allows users to fabricate complex 3D structures. The invention of DMD and LcoS panels pushed the resolution to a higher level since they have smaller pixel size and higher filling ratio (89% to 92%). In 1999, X. Zhang et al. used the DMD chip to fabricate micron scale polymeric and ceramic microstructures [24]. Nowadays, this method is extensively used to fabricate engineered tissues or vascular networks for biomedical applications [25-27]. In this study, we chose to use the DMD chip because the pixel size is small enough with the projection lens to generate the resolution that can fulfill the requirement for the fabrication and it has a better UV compatibility and is more cost-effective than LcoS.

2.2 Working principle of DMD

The DMD has 1024 × 768 of micro mirrors arrayed on the chip and each of these mirrors has the dimension of 17 μm × 17 μm. One micro mirror represents a single pixel on the DMD chip and an example image of two pixels is shown in Figure 2.1. The DMD is an opto-mechanical device because the light reflection is determined by tilting angle of each pixel. Every micro mirror on the chip has two stable states: the "on" state in which one mirror is tilted +12 degrees of its own yoke axis, and the "off" state in which the mirror is tilted -12 degrees to the axis. The numbers of 1 and 0 show the two different states of these micro mirrors. Only the light reflected from the mirrors' "on" state will be collected by the projection lens and on the contrary, the mirrors' "off" state will deflect the light to elsewhere. In this way, users can project any patterns by controlling these micro mirrors' "on" and "off" states. In practice, the pattern shown on a DMD chip is synchronized with the display of the computer monitor.

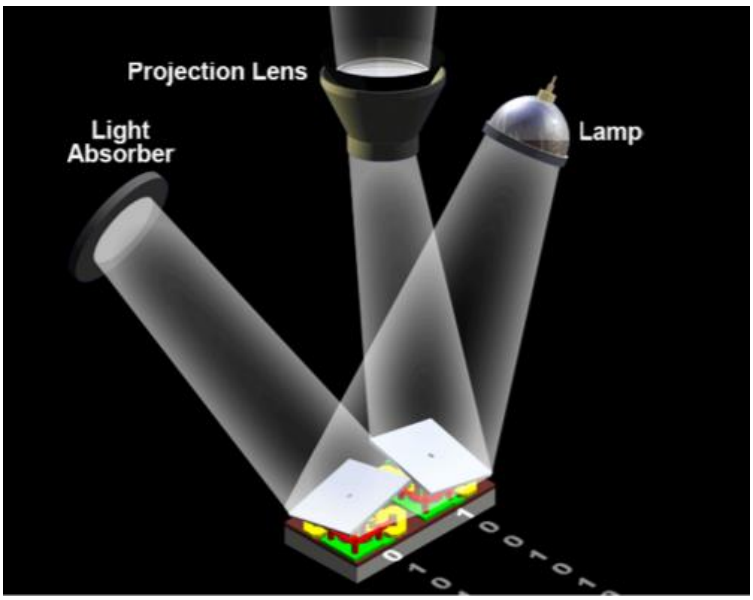

Figure 2.1 Schematic of micro mirrors on a DMD chip [1].

2.3 System design

2.3.1 Optics design

The DMD chip that we use for this study is dissembled and engineered from a commercial projector (Lp435z, Infocus Inc.). It contains 1024 × 768 micro mirrors and the diagonal length is 0.9 inch. An 80 mW UV LED with 365 nm wavelength (LCS-0365-02-11, Mightex Inc.) is the light source of the system and is powered by a power supply (hp6622a, HP). In order to improve the uniformity of light output, diffusers are fixed after the UV LED. A condenser (A143, Raymond optolife Inc.) is set after the diffusers to expand the UV spot so that only the center part of the light spot will shine on the DMD chip, further making the illumination intensity uniform. Because the tilting angle of each micro mirror is 12 degrees along the diagonal line, the direction of the light is set as 12 degrees to the normal direction of these "on" state mirrors. By contrast, the light illuminating the "off" state mirrors will be collected elsewhere and will not enter the main optical path. The pattern on the DMD is controlled with MATLAB. Every single pixel of the pattern is a value between 0 and 1 in the MATLAB code and the value indicates the grayscale intensity, where 1 has the highest illumination and 0 is totally dark. The grayscale control of every pixel can further improve the illumination uniformity by lowering the grayscale value at relative brighter areas. The DMD chip is set at the focal length of a lens so that we expect to get parallel light. The light is reflected by a beam splitter and then enters the projection lens (10 ×, NA = 0.3, Nikon) which focuses the pattern at the upper surface of the glass. The size of a single pixel is 17 μm by 17 μm so that theoretically the resolution can reach 1.7 μm. The pattern at the upper surface of the glass slide is reflected onto the projection lens and is focused by another lens into the CCD camera (T3, Canon). Figure 2.2 is the schematic of the set up.

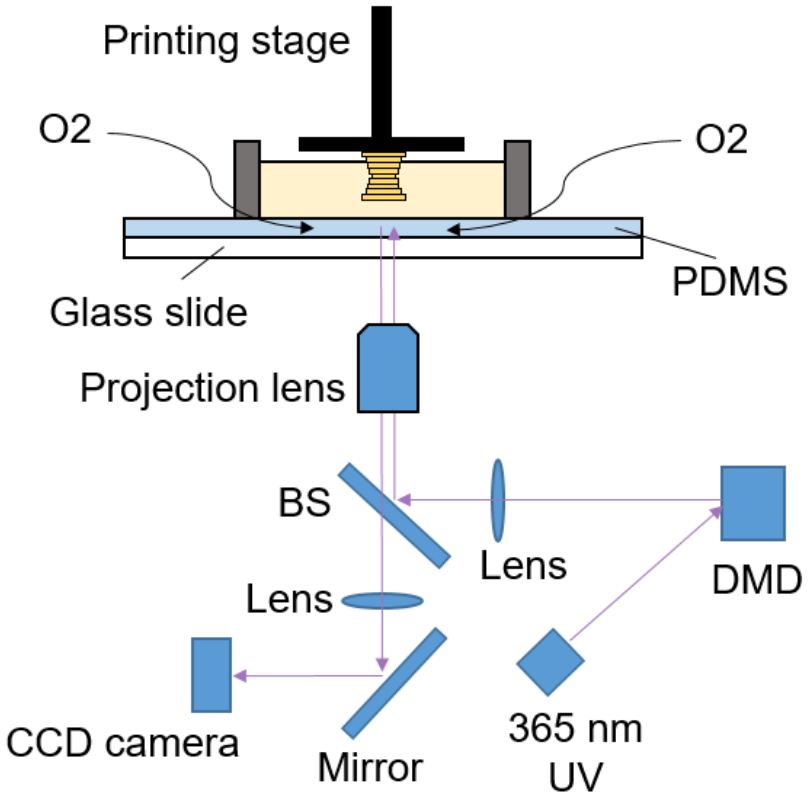

Figure 2.2 Schematic of set up

2.3.2 Motion design

The system set up is shown in figure 2.3. The moving parts of the 3D printing system include a XY stage and a Z stage. The control of the motion for both stages is by LabVIEW. The glass slide is mounted on a XY stage as the substrate for the printing materials. The motion of the XY stage allows exposure at various areas and is mainly used for the initial study of properties of materials. The XY stage needs to be adjusted perpendicular to the incident light. A small piece of mirror replaced the projection lens and the position of the image of CCD camera is recorded. And then the mirror was put at the surface of the glass slide, the level of the XY stage was adjusted until the image in the CCD camera reaches the same position that was recorded before. In this way,

we can always maintain the substrate level to be perpendicular to the incident light. To realize 3D printing, a Z stage is mounted independently with XY stage to control the printing substrate where the structure will be fabricated. Instead of using the method of top down that printing stage move from top to the bottom, the bottom up method is used in this study for the following reasons: (1) There will be no limitation of the height of the printed structure since the Z-stage can move up with any specific distance. (2) Better control of the interface between the surface of the solution with the illumination. The bottom up method can always keep the surface of the solution contacted with the substrate flatly. (3) This method is more cost-effective because the printed part will be lifted out of the solution that less material is required. The printing substrate is made with a metal rod where the top is attached with the replaceable circle glass slide of 12 mm diameter. The 3D printing process begins with sinking the printing substrate into the prepolymer solution till it contacts with the solution substrate and then it will be lifted one-layer thickness.

2.3.3 Solution substrate

The solution substrate is where the printing material is placed on. Because the bottom up method is used, the printed structure should only adhere to the printing substrate but not to the substrate that holds the prepolymer solution. In order to avoid stickiness, oxygen-permeable film is attached onto the solution substrate [28, 29]. There are two kinds of films used in this study, the first is a thin layer of PDMS coated on the 3 inch × 3 inch glass slide. The second one is a stretched Teflon AF 2400 film (Biogeneral Inc). They both allow for the diffusion of oxygen into the film and at the bottom region of the solution. Oxygen acts as a free radical quencher and will compete with the radical production reaction. The oxygen inhibition mechanism creates a thin, unpolymerized layer that is formed at the bottom of the prepolymer solution. In this way, the

polymerized layer will not stick with the solution substrate. The detail of the mechanism will be explained in the next chapter.

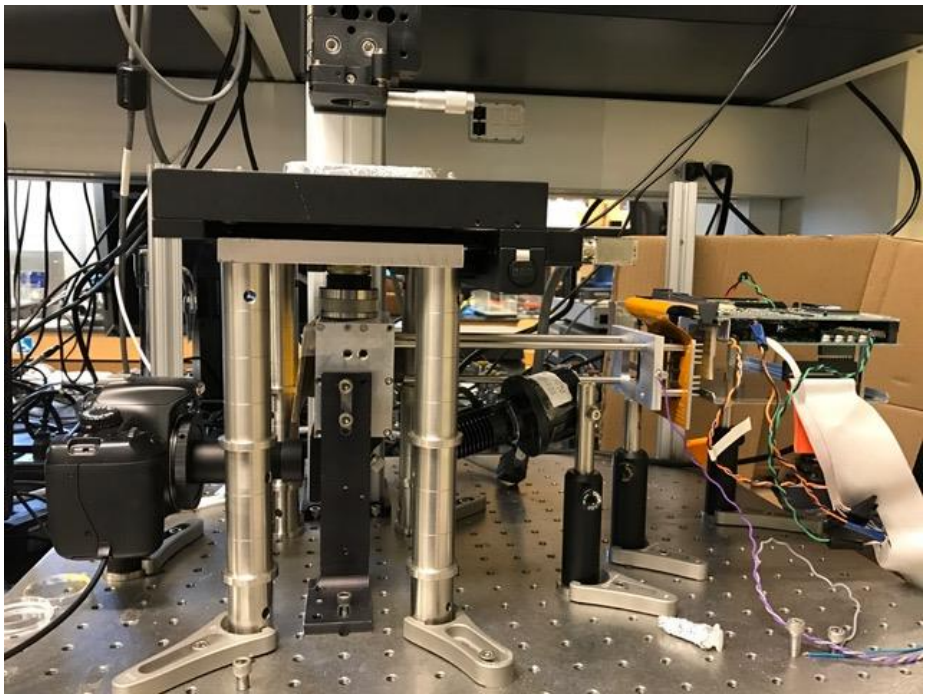

Figure 2.3 System set up

Chapter 3 Modeling the effect of oxygen inhibition in 3D printing

3.1 Introduction

There are two major methods of stereolithography in terms of the printing direction [30]. The first is the top down method where the fresh layer always forms at the thin slice between the previous formed layer and the open air, and the printing stage sink downward in Z direction. The second is the bottom up method where the fresh layer is always formed between the solution substrate and the previous formed layer, and the printing stage goes upward in Z direction. In this study, the bottom up method has been used and the advantages have been illustrated in the previous chapter. For the bottom up method, the fresh formed layer can stick to the solution substrate and hinder the ongoing 3D printing. To solve this problem, people used a thin layer of oxygen permeable film as the solution substrate [29]. The oxygen inhibition reaction is usually faster than the radical production and in a result, a thin layer of unpolymerized prepolymer between the printing substrate and the fresh layer will be formed. Previously, a 1-D comprehensive kinetic photopolymerization model is applied to simulate experimental conditions and study the impact of oxygen on photo-polymerization kinetics [31]. The oxygen-inhibition mechanism is also used to predict the kinetics on continuous flow lithography [32]. Based on the previous study, we included the effect of light absorber and developed the kinetic model for our own system.

3.2 Materials

3.2.1 Oligomer

Among PEG based hydrogels, Poly(ethylene glycol) dimethacrylate (PEGDMA) 750 Da is used as our prepolymer because it has better strength and durability than other multiacrylate counterparts. Although it may polymerize more slowly, it can form a stronger polymer with higher glass transition. It also has shorter chains which can provide a large space for controlling the crosslinking degree so that polymers with a larger range values of elasticity can be made.

3.2.2 Photoinitiator

Currently, the UV initiator 1-[4-(2-hydroxyethoxy)-phenyl]-2-hydroxy-2-methyl-1-propanone (Irgacure 2959 or I2959 from Ciba Specialty Chemicals, Tarrytown, NY) is the most commonly used photoinitiator for cellular encapsulation within hydrogels [33-35]. But in this study, two other kinds of photoinitiators have been used because they have different advantages respectively. The first one is lithium phenyl-2,4,6-trimethylbenzoylphosphinate (LAP). LAP is used as the photoinitiator because of the following reasons [36]: 1) The wavelength of our UV light source is 365 nm. LAP has a much larger absorption at around this range. The time required to reach the gel point during the solution polymerization of PEGDMA is approximately one order of magnitude lower for LAP than for I2959 with 365 nm illumination at comparable intensities and initiator concentrations. 2) Compared to the solubility of I2959 in water (2%), LAP has a larger solubility (up to 8%), so we can make different concentrations of PEGDMA in water, which is a method to control the polymer strength. 3) The same concentration of LAP and I2959 has been proven to have nearly identical cytocompatibility. The second photoinitiator that has been used is Phenylbis 2,4,6-trimethylbenzoylphosphine oxide (I819). It has high absorbance at a range of 365

nm and compared to LAP, the solubility of I819 in PEGDMA is much higher. In 100% PEGDMA solution, I819 is used because LAP is nearly not dissolved at all. When PEGDMA is dissolved into water with different concentrations, LAP will be used because I819 has low solubility in water.

3.2.3 Light Absorber

The layer thickness determines the vertical resolution of the 3D printed structure. According to the Beer-Lambert law, the light intensity equals:

$$I(z) = I_0 exp(-\frac{z}{D_p}) \tag{3.1}$$

$$D_p = \frac{1}{\varepsilon_d[D] + \varepsilon_i[S]} \tag{3.2}$$

where I_0 is the light intensity at the surface of the solution, D_p is the light penetration depth in the solution, ε_d is the molar extinction coefficient of the photoinitiator, [D] is the concentration of photoinitiator, ε_i is the molar extinction coefficient of the light absorber, [S] is the concentration of the light absorber. The material used for light absorber is TINUVIN 234 in this study.

3.2.4 Preparation of printing substrate

The printing substrate in the study is a circle glass slide with a 12mm diameter (Ted Pella, Inc). If the glass slide is directly used for printing, the printed structure will fall off. In order to increase the adhesion of the printing substrate, glass slides go through several steps for preprocessing before the printing. At first, the glass slides are cleaned for 15 minutes in acetone solution in ultrasound bath. Then the coverslips are taken out of the acetone and cleaned with ethanol for another 15 minutes. In the meantime, a methacrylation solution is prepared by mixing together 1mL 3-(trimethoxysilyl)-propyl methacrylate, 50mL ethanol, and 6mL of 1:10 glacial

acetic acid (acetic acid in ethanol). The glass slides are dried and immersed in the methacrylation solution for 2-3 hours. After this, the glass slides are taken out of the methacrylation solution and are cleaned with ethanol twice and dried. The preprocessed glass slides are then stored in a refrigerator under the temperature range of 1-4 degrees C.

3.2.5 Preparation of PDMS spin coated substrate

At first the PDMS solution and the agent are mixed at a volume ratio of 10:1 and then the mixture is continuously stirred for 2 to 3 minutes to mix completely. This mixture is then put on the clean glass slide that goes through a wash of IPA and DI water. The glass slide with the mixture is then sealed in a vacuum chamber and a pump is used to get rid of the air in the solution. The spin coating speed is set to 2000 rpm for 5 minutes to get a 10 μm thick PDMS thin layer. After the spin coating process is done, the glass slide is put on a hot plate at 70 degrees C for 15 minutes. And it is put in the fume hood overnight for further drying.

3.3 Reaction mechanism

The simulation is based on the free radical polymerization and the oxygen inhibition process. In table 3-1, the whole process of the polymerization is illustrated.

In step I, the photoinitiator absorbs the light and photocleaves into radicals. The initiated radicals break the double carbon bond and form primary radicals in step II. Then the primary radicals propagate with other oligomers to create polymer networks in step III and IV. Next, the termination of the propagation occurs when two primary radicals react and form a dead polymer chain in step V. Oxygen is a kind of radical quencher that reacts with free radicals and inhibits the crosslinking process which is shown in step VI. This process is much faster than the propagation

rate of polymerization so that the polymerization usually happens when the oxygen in the solution is depleted.

Initiation:	$I + h\nu$	$\rightarrow$	$2I^{\bullet}$	[I]
	$I^{\bullet} + R'CH{=}CH_2$	$\rightarrow$	$R'C^{\bullet}H{-}CH_2{-}I$	[II]
Propagation:	$R'C^{\bullet}H{-}CH_2{-}I + R'CH{=}CH_2$	$\rightarrow$	$R'CH{-}CH_2\text{-}I$ $\vert$ $R'C^{\bullet}H{-}CH_2$	[III]
	$(R'CH{-}CH_2\text{-}X)_n + R'CH{=}CH_2$ $\vert$ $R'C^{\bullet}H{-}CH_2$	$\rightarrow$	$(R'CH{-}CH_2\text{-}X)_{n+1}$ $\vert$ $R'C^{\bullet}H{-}CH_2$	[IV]
Termination	$(R'CH{-}CH_2\text{-}X)_n$ $\vert$ $R'C^{\bullet}H{-}CH_2$ + $(R'CH{-}CH_2\text{-}X)_n$ $\vert$ $R'C^{\bullet}H{-}CH_2$	$\rightarrow$	Dead Polymer	[V]
Oxygen	$X^{\bullet} + O_2$	$\rightarrow$	$XO_2^{\bullet}$	[VI]

Table 3-1 Mechanism of free radical photopolymerization [37].

3.4 Model description

In the first step, the UV light shines into the prepolymer solution and induces the photocleavage process of photoinitiators, producing primary free radicals in the process. The rate of radical generation is proportional to the absorption rate of incident photons. In a thin slice thickness at a height z, the volumetric rate of absorption r_a is given by:

$$r_a = -\varphi \frac{\partial I(z)}{\partial z} \tag{3.3}$$

where I(z) is the light intensity, and φ is the quantum yield of formation of initiating radicals with the incident photons. According to Beer-Lambert's law, the light intensity changes through the solution and is given by:

$$\frac{\partial I(z)}{\partial z} = -\varepsilon[PI]I(z) \tag{3.4}$$

where ε is the molar extinction coefficient of the photoinitiator and [PI] is the concentration of the photoinitiator. And then the rate of radical production can be expressed as:

$$r_a = \varphi\varepsilon[PI]I_0 exp(-\varepsilon[PI]z) \tag{3.5}$$

In the second step, a radical species consumes one molecule of M to form a larger radical. And the propagation rate constant is given by k_p. Radicals are consumed through two different reactions. The first occurs when two radical species react with each other and terminate the propagation to form a longer chain. The termination rate constant is k_t. The second occurs during the reaction with oxygen. The rate constant is k_o. The rate of radical consumption, r_c, is given by:

$$r_c = k_t[\dot{X}]^2 + k_O[\dot{X}][O_2] \tag{3.6}$$

The propagation will only happen when the rate of radical generation is equal to radical consumption, so that it is assumed that $r_c = r_a$, then the concentration of radicals can be expressed by the equation:

$$[\dot{X}] = \frac{-k_O[O_2] + \sqrt{(k_O[O_2])^2 + 4r_a k_t}}{2k_t} \tag{3.7}$$

The change of the concentration of oxygen is determined by the diffusion of oxygen from the substrate and the consumption with the radicals

$$\frac{\partial[O_2]}{\partial t} = D_O \frac{\partial^2[O_2]}{\partial z^2} - k_O[O_2][\dot{X}] \tag{3.8}$$

$$\theta = \frac{[O_2]}{[O_{2,eqb}]}, \qquad D_{a1} = \frac{{k_O}^2 H^2[O_{2,eqb}]}{2k_t D_O}$$

$$\alpha = \frac{4\varphi\varepsilon[PI]I_0 k_t}{{k_O}^2[O_{2,eqb}]^2}, \qquad \beta = \varepsilon[PI]H$$

where D_o is the diffusivity of the oxygen and $[O_2, eqb]$ is the concentration of oxygen at the surface of the substrate. H is the depth into the solution and D_{a1} is the damkohler number that determines the ratio between oxygen termination with the diffusion of oxygen. Nondimensionalizing equation 3.7 and 3.8, we can find the change of oxygen concentration in the solution as the function of time and depth:

$$\frac{H^2}{D_O}\frac{\partial\theta}{\partial t} = H^2\frac{\partial^2\theta}{\partial z^2} - Da_1\theta(-\theta + \sqrt{\theta^2 + \alpha\, exp\left(\frac{-\beta z}{H}\right)}) \tag{3.9}$$

The boundary conditions for this equation are:

$$\theta(0,t) = 1$$

$$\theta(z,0) = 1 \tag{3.10}$$

Since the diffusivity of oxygen in Teflon film is at least 2 orders of magnitude greater than that in the PEGDMA solution, the concentration of oxygen is assumed to be the same as the $[O_2, eqb]$ at the interface between the Teflon film and the prepolymer solution. It is also assumed that at the beginning of the reaction, the oxygen concentration is at the equilibrium everywhere in the oligomer solution.

During the polymerization, the unconverted double bonds are consumed in the chain propagation step while the concentration of radicals is unaffected. The concentration of unconverted double bonds is given by

$$-\frac{\partial[M]}{\partial t} = k_p[M][\dot{X}] \tag{3.11}$$

Nondimensionalizing equation 3.11 using

$$\xi = \frac{[M]}{[M_0]}, \qquad D_{a2} = \frac{k_p k_O [O_{2,eqb}] H^2}{2 k_t D_O}$$

where $[M_0]$ is the initial concentration of unconverted double bonds, ξ is the fraction of the remaining unconverted double bonds, D_{a2} is a dimensionless Damkohler number that determines the ratio of the rate of radical propagation to the diffusion of oxygen into the prepolymer solution. We can obtain the conversion rate of the polymerization process as:

$$-\frac{\partial \xi}{\partial t} = Da_2 \xi \left(-\theta + \sqrt{\theta^2 + \alpha \, exp\left(\frac{-\beta z}{H}\right)}\right) \tag{3.12}$$

Since no conversion happens before the polymerization, the boundary condition is

$$\xi(z, 0) = 1 \tag{3.13}$$

The time-varying profile of θ and ξ with exposure time is shown in figure 3.1 and the parameters for calculation are in table 3-2.

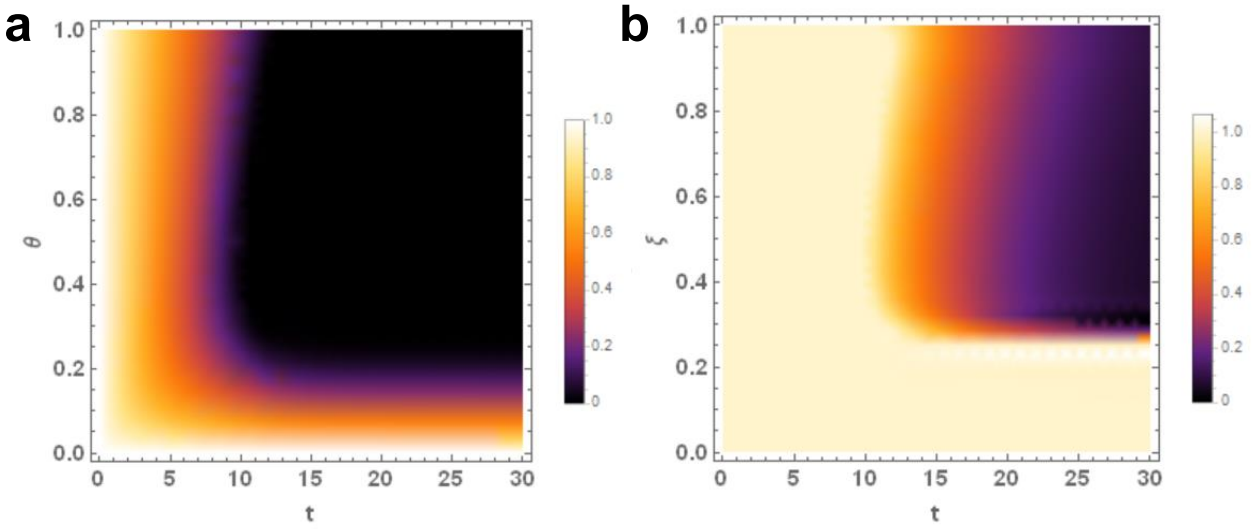

Figure 3.1 Time varying profile of (a) θ and (b) ξ with exposure time

Parameter	Value	Unit	Reference
k_p	25	$m^3/(mol\ s)$	[38]
k_t	2520	$m^3/(mol\ s)$	[38]
k_O	5×10^5	$m^3/(mol\ s)$	[39]
D_O	2.84×10^{-11}	m^2/s	[40]
H	80	μm	Measured
I_0	3.0×10^{-4}	$E/(m^2\ s)$	Measured
[PI]	23.9	mol/m^3	Measured
ε_{PI}	30	$m^3/(mol\ m)$	[41]
[LA]	15.8	mol/m^3	Measured
ε_{LA}	315.8	$m^3/(mol\ m)$	[42]
$[O_{2,eqb}]$	1.0	mol/m^3	[43]
φ	0.6	-	[44]

Table 3-2 Parameters used for calculation

Chapter 4 Characterization of the system

4.1 Introduction

The characterization of the 3D printing system relates to the printing speed and resolution. The printing speed is mainly determined by the time that materials need to be solidified. Due to the symmetry of X and Y direction at the printing plane, the resolution will be characterized at the XY plane and Z direction. The following is the characterization of the stereolithography system, including effect of components in the materials, layer thickness control and resolution.

4.2 Role of photoinitiator

For chain polymerizations that have non-chain length-dependent bimolecular termination, the rate of polymerization is usually proportional to the square root of initiation rate, R_i [45]. $R_i = \frac{2\varphi\varepsilon f I C_i}{N_A h\nu}$, where C_i is the concentration of photoinitiator, I is the light intensity, φ is the quantum yield, ε is the molar extinction coefficient of the photoinitiator, and f is the photoinitiator efficiency, or the ratio of initiation events to radicals generated by photolysis. Avogadro's number, N_A; Plank's constant, h and the frequency of the initiating light, ν are included for unit conversion. This equation describes how parameters affect the polymerization rate. In the experiment, the molar extinction coefficient and the concentration of the photoinitiator are related with the materials, and the light intensity can be tuned to a proper value in order to better control the gelation time. In figure 4.1, the gelation time for three different concentrations of photoinitiator with various exposure areas are plotted. The higher the concentration, the faster the polymerization rate.

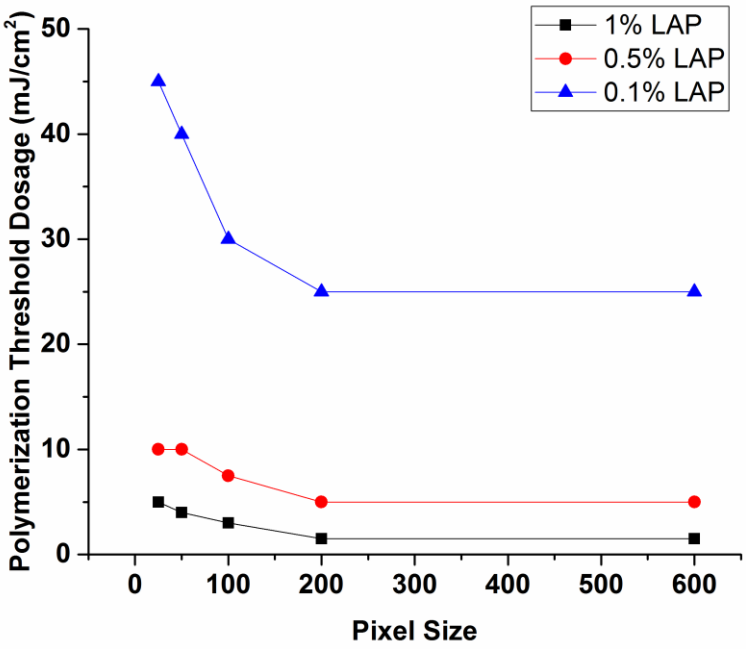

Figure 4.1 Polymerization threshold dosage with various pixel size and concentrations of photoinitiators.

4.3 Role of light absorber

The vertical resolution is determined by the thickness of polymerization in vertical direction that is called curing depth. The curing depth is related to energy dosage at the exposure area. When the energy dosage exceeds the critical value, the polymerization begins. The curing depth C_d can be calculated by: $C_d = D_p \ln(\frac{E_0}{E_c})$, where E_c is the critical dosage of the polymerization and E_0 is the dosage at the exposure area. From the equation, the lower the light penetration, the smaller the curing depth. The light absorber has a much larger molar extinction coefficient, which will affect the light penetration the most compared to other components in the solution. In this way, solutions with various concentrations of light absorber are used to polymerize the same size of square area that is ~1mm^2. The exposure time varies from 1 second to 2.2 seconds

with 0.2s step. The light intensity is $5\mathrm{mW/cm^2}$. The height of each sample is measured by profilometer and the result is shown in figure 4.2. The higher the concentration of the doping, the thinner the sample that can be printed under the same energy dosage.

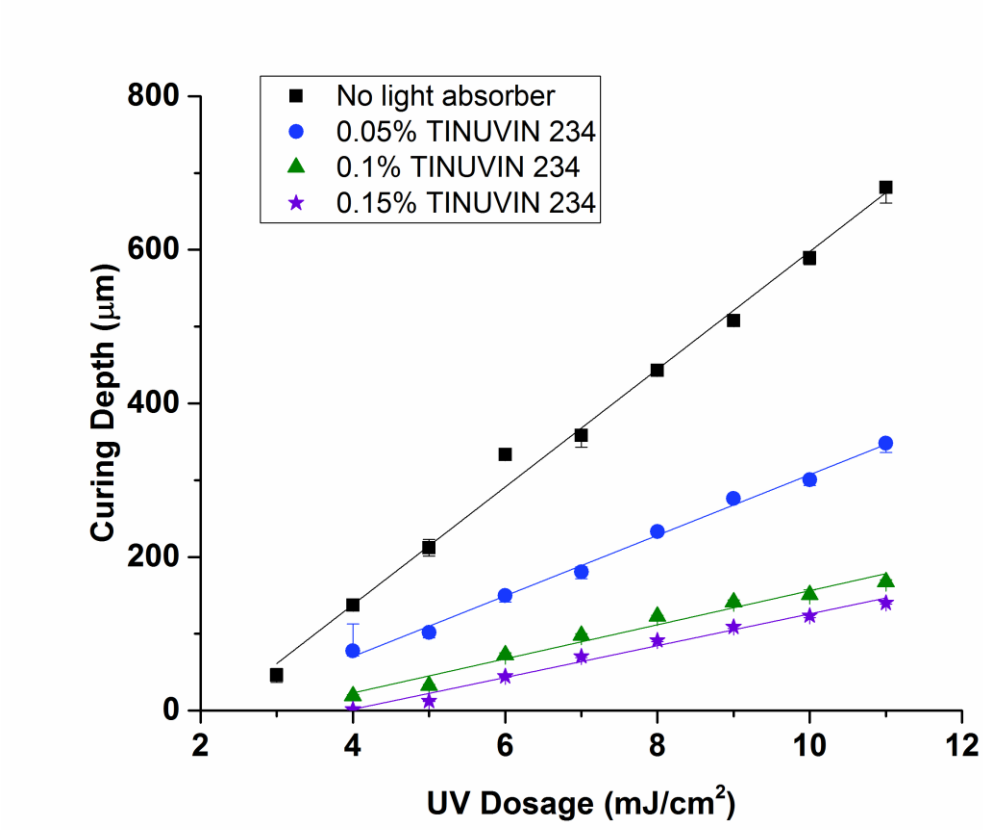

Figure 4.2 Curing depth with UV dosage and concentrations of light absorber

4.4 Layer thickness control

To make true 3D printed structures, not only do we need to know the curing depth of 2D printing, but we also must measure the curing depth in 3D. In this work, the bottom up method was used and the advantages of it have been described in the beginning of the chapter. If a single piece of glass slide is used as the substrate for the prepolymer solution, then the freshly formed layer will be stuck at the substrate and hinder the ongoing 3D printing. So, a thin layer of oxygen permeable film is either coated or stuck on the glass slide to permit the formation of an un-crosslinked layer. The oxygen permeable film is used with a thin layer of PDMS (~20 μm) or a thin film of Teflon AF 2400 film. In the example shown below, Teflon film is used. 100% PEGDMA, 0.3% I819 and 0.5% TINUVIN 234 is used as prepolymer solution. Figure 4.3 (a) is a SEM image of a multilayer structure and (b) shows the thickness of 5 suspended layers.

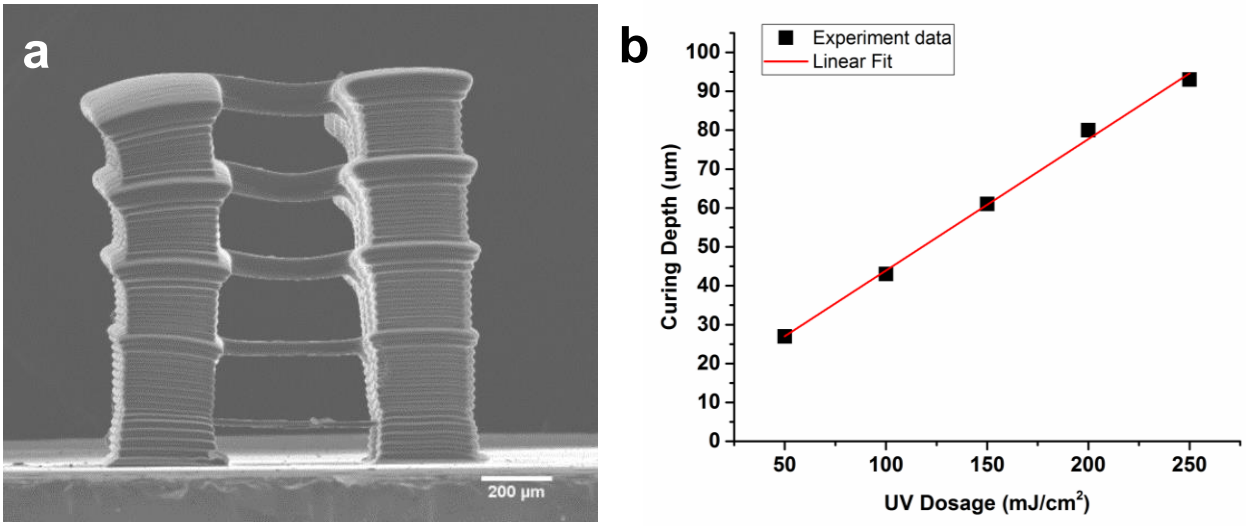

Figure 4.3 (a) SEM image of a multilayer structure. (b) Layer thickness of suspended bridges.

4.5 Resolution test

To investigate the resolution in projection plane, lines with different spatial frequencies are designed and printed. Two kinds of materials were used in this research. The first one is SU 8. SU 8 is a common epoxy-based negative photoresist. The design of the exposure sequence is shown in figure 4.4. The area that is exposed to light becomes crosslinked, and the other area remains soluble and is washed away during the development process. In figure 4.5, the image of lines with 10 pixels spacing is shown. The following is the process of resolution test for SU 8.

(1) Substrate pretreat: Si wafer was cut into small square chips with dimensions of 1 cm^2 which were used as substrate for the printing. Then substrate was cleaned by piranha solution (H_2SO_4 & H_2O_2), followed cleaning by Acetone, IPA for 5 minutes each, and then rinsed by de-ionized water.

(2) Spin coating: The SU 8 was dispensed onto the surface of the substrate. Spin coated the substrate for 30 s with 2000 rpm.

(3) Soft bake: The substrate was put on a hot plate for soft bake with 95 degrees C for 1 minute.

(4) Expose: The substrate was inverted mounted on the printing stage. The exposure time varied from 10s to 120s. The power density used was 5 mW/cm^2 and 10 mW/cm^2 respectively. Figure 2.8 shows the idea of multi-exposure steps. In the horizontal line, the line width was designed to be the same while the exposure time was increasing. In the vertical direction, the exposure time was kept the same while the line width was increasing. In this way, the optimized condition for the finest resolution can be obtained.

(5) Post exposure bake: After the exposure, the substrate was put on the hot plate for post exposure bake at 95 degrees C for 1 minute. Then a latent image of the exposure area should be visible.

(6) Development: Immerse the substrate into the developer for 10 seconds, followed by the wash with IPA. The result is shown in figure 2.8. The minimum line width that can be printed is 10 pixels. If the spatial frequency is down to 5 pixels, the lines will not completely separate. The resolution of the system with SU 8 was 20 microns.

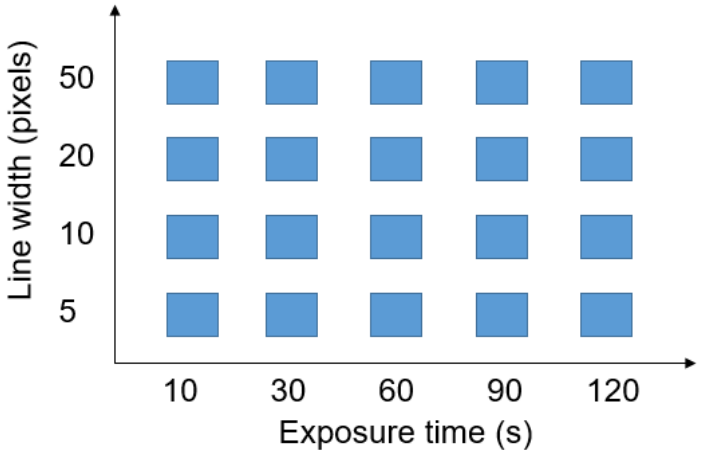

Figure 4.4 Schematic of exposure sequence of SU 8

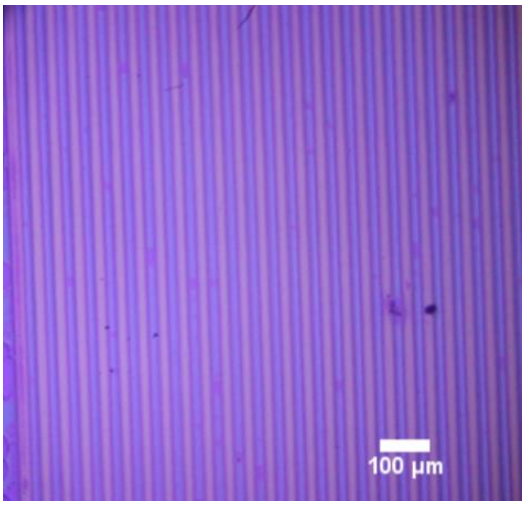

Figure 4.5 Digital image of lines with 10 pixels spacing

The resolution was tested with PEGDMA. The patterns used for printing are the same as the various spatially frequent stripes. The height of the solution is limited by the double-sided tape,

which is 50 μm measured with calibrator. The PEGDMA solution is added from the side and forms a thin layer of solution with the help of capillary force. Then the glass substrate is mounted on the printing stage. The resolution of PEGDMA is better than SU8 because the oxygen acts as a radical quencher and reacts with free radicals, which terminates the polymerization process. The oxygen consumption process competes with the process of radical generation. The polymerization will only happen when the speed of generation of radicals is larger than the consumption of oxygen. This mechanism allows thinner lines to be printed compared with SU 8. The image of lines with a spacing of 5 pixels is shown in figure 4.6.

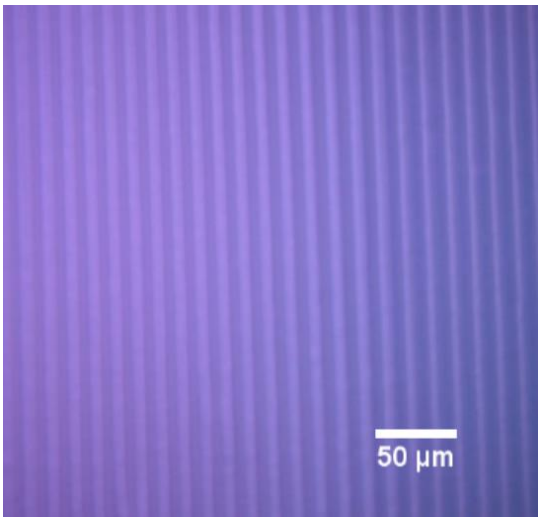

Figure 4.6 Digital image of lines with 5 pixels spacing

4.6 3D printing process

The printing process can be divided into three steps, as shown in figure 4.7. The first step is to slice the 3D model with Solidworks and get the cross-section images. The number of the images is determined by the layer thickness. Once the images have been saved in a file, they will be set as mask and can be exposed one by one, which is controlled by the LabVIEW program. After the printing steps complete, the circle slide as the printing stage is taken off from the Z stage and put in the ethanol solution bath for 12 hours. Figure 4.8 (a) and (b) are two example images.

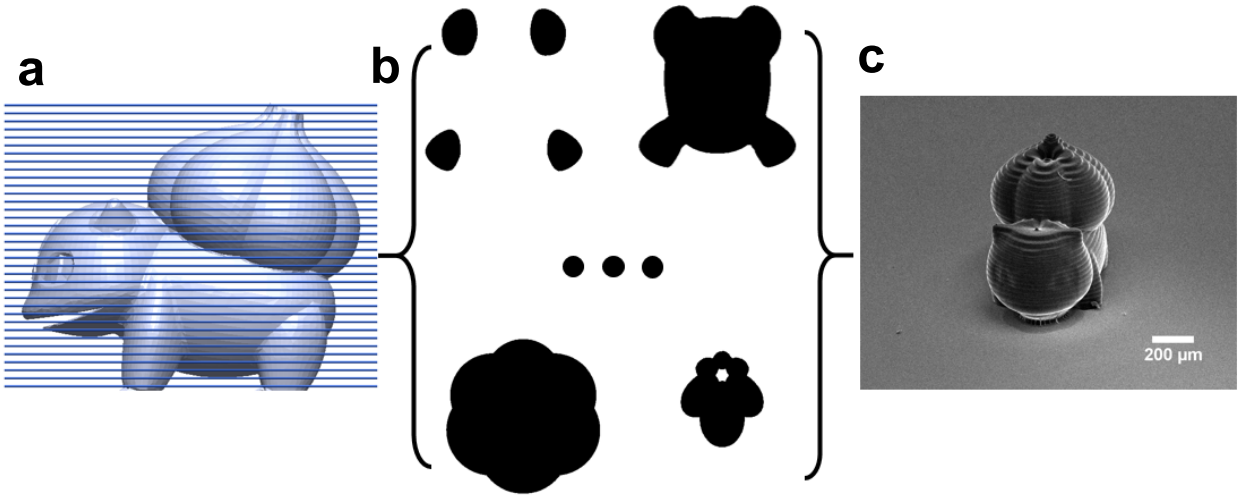

Figure 4.7 3D printing process with (a) Slicing the 3D model into cross-section images. (b) Expose sliced images. (c) Develop and obtain the 3D structure.

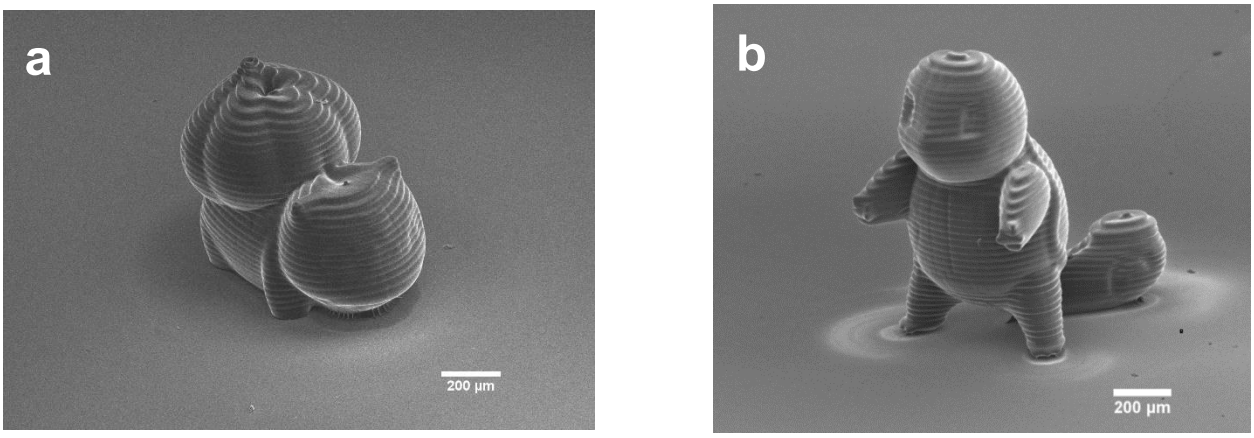

Figure 4.8 SEM image of 3D printed (a) bulbasaur and (b) squirtle

Structures are then printed to check the printing capability of thin rods and tubes. In figure 4.7 (a), rods with different diameters have been fabricated. The thinnest rod that can be printed and remain standing has the diameter of 40 μm. Figure 4.7 (b) shows tubes with different diameters. The outer diameter can reach 60 μm and the inner diameter can reach 30 μm.

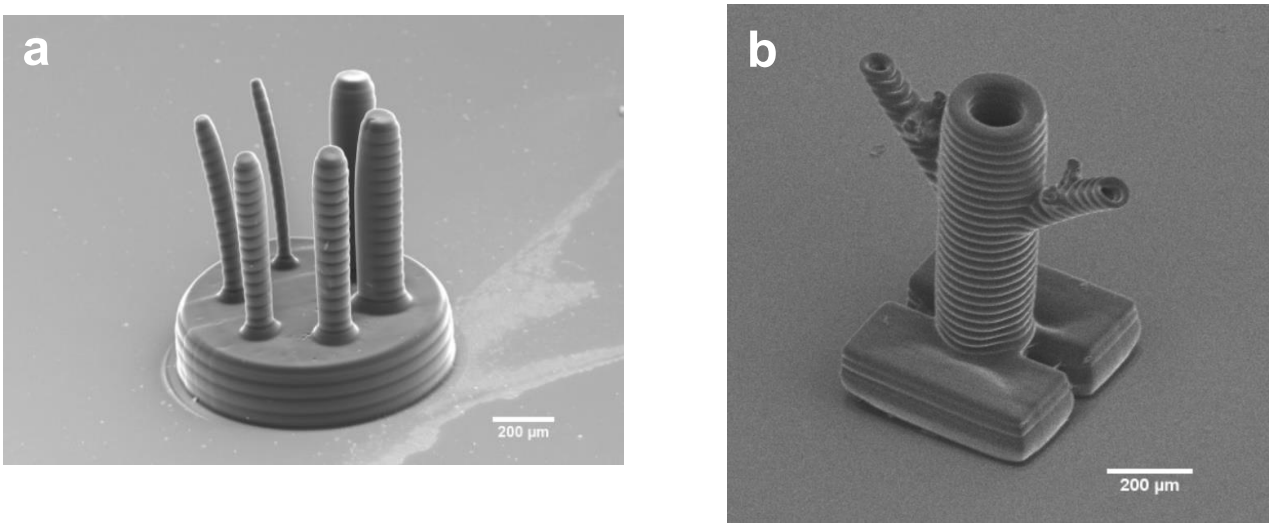

Figure 4.7 SEM image of (a) standing rods and (b) vascular structure

Chapter 5 Fabrication of 3D structures with stiffness control

5.1 Introduction

Cells can sense stiffness of the surrounding extracellular matrix (ECM) and can react to these environments by changing their organization and migration [7, 8]. The phenomenon of durotaxis has been well studied, indicating that most normal cells migrate up the rigidity gradient in the direction of greater stiffness [46]. Over the last decade, considerable advances have emerged in microfabrication techniques for generating structures with a well-defined stiffness gradient that influences cellular responses at micro and sub-micro scales [47, 48]. For instance, a wide range of matrix stiffness will influence the focal-adhesion structure and the cytoskeleton of differentiated cells [9]. Additionally, stripes of hydrogel structures with various stiffness were constructed and human mesenchymal stem cells were observed to congregate in the softest region of the gel [18]. However, most of the studies focus on the 2D control of matrix stiffness; the challenge remains in fabricating 3D structures with controlled stiffness.

The PEG-based hydrogel has been extensively used for biomedical applications not only owing to its biocompatibility but also its easily tuned mechanical properties [49, 50]. The stiffness of PEG-based hydrogel is largely dependent on the crosslink density. Light-based 3D printing methods using photopolymerization mechanisms can locally control the stiffness by controlling the energy dosage to further induce or degrade the crosslink [20, 51]. To date, light-based 3D printing methods have been limited to using physical masks, dynamic masks and laser scanning methods. A physical mask is designed to block light at specific regions so that it can control the stiffness [52]. Although this is a straight forward method, the complex 3D structure may need to use different designs of masks. Another method of the dynamic mask was introduced to control

the light intensity with gray scale pattering [16]. However, this 3D printing method was used to only create stiffness gradient 2D structures for biomedical applications [18]. Laser scanning methods can induce the change of crosslink density of hydrogel structures in 3D, but the efficiency is low and it requires the post treatment after the first-time fabrication [19, 20]. Thus, a 3D printing method with high-resolution control over stiffness without post treatment is in need.

Here, we developed a gray scale printing method to fabricate 3D structures with well-controlled stiffness using a projection stereolithography system. Compared to other lithography technologies such as physical photomask lithography and two photon lithography, the Digital Micro-Mirror Device (DMD) based technology provides a higher degree of efficiency by controlling nearly a million micro mirrors at the same time. And the control of each mirror's gray scale allows for a pattern with gradient crosslink density with a single exposure. Although people have been using DMD-based technology to make 3D structures [13] or gray scale patterning in 2D [18], applying the technology to control the stiffness for 3D structures is still rare. Here, we propose a method to tune the stiffness of hydrogel structures in 3D. Atomic Force Microscope (AFM) was used to quantitatively determine the relationship between the power density used and the elasticity of hydrogel. Furthermore, qualitative images of hydrogel structures with the same geometrical appearance but different stiffnesses are demonstrated. Finally, cells were seeded on the printed 3D structures and the control over the organization of smooth muscle cells were realized.

5.2 Grayscale printing

The schematic of the stereolithography setup is shown in figure 5.1 (a). The DMD chip can form user-defined patterns with nearly a million micro-reflecting mirrors. By controlling the grayscale of these micro mirrors, the fluctuating frequency of each mirror can be regulated. When the UV light illuminates the DMD chip, the mirrors fluctuate in high frequency and reflect higher dosage of energy and vice versa. Thus, an image with spatially regulated power density is collected by the projection lens and then focused onto the substrate of the prepolymer tank.

The prepolymer solution used in this work is 80% poly(ethylene glycol) dimethacrylate (PEGDMA) in DI water. The UV light initiates the polymerization and the grayscale display of DMD chip, spatially controlling the crosslinking density of the polymer. Figure 5.1(b) was made with different grayscales and an obvious optical contrast between areas can be observed under a bright field microscope. The power density for the brighter area was 15 $\mathrm{mW/cm^2}$ while the darker area was 5 $\mathrm{mW/cm^2}$ and the exposure times for both were 5 seconds. It was anticipated that under the same exposure time, the higher the power intensity, the greater the crosslinking density will occur.

In order to study how stiffness independently affects cellular behaviors, other factors have to be eliminated, such as geometrical difference. Although higher dosages will cause taller heights, as long as the difference falls within a certain range, the effect of the difference can be ignored. Figure 5.1(c) illustrates the scattering intensity map of a single line across the microscope image and clear peaks can be observed at every cross point with brighter area. While at the same place, profilometer was used to measure the surface roughness. In figure 5.1(c), the difference of the height is within a range of 5 μm which is a comparable size with cell size. Thus, changing the

grayscale of the pattern while keeping the same exposure time is a promising method for making geometrically similar structures with different stiffnesses for tissue engineering.

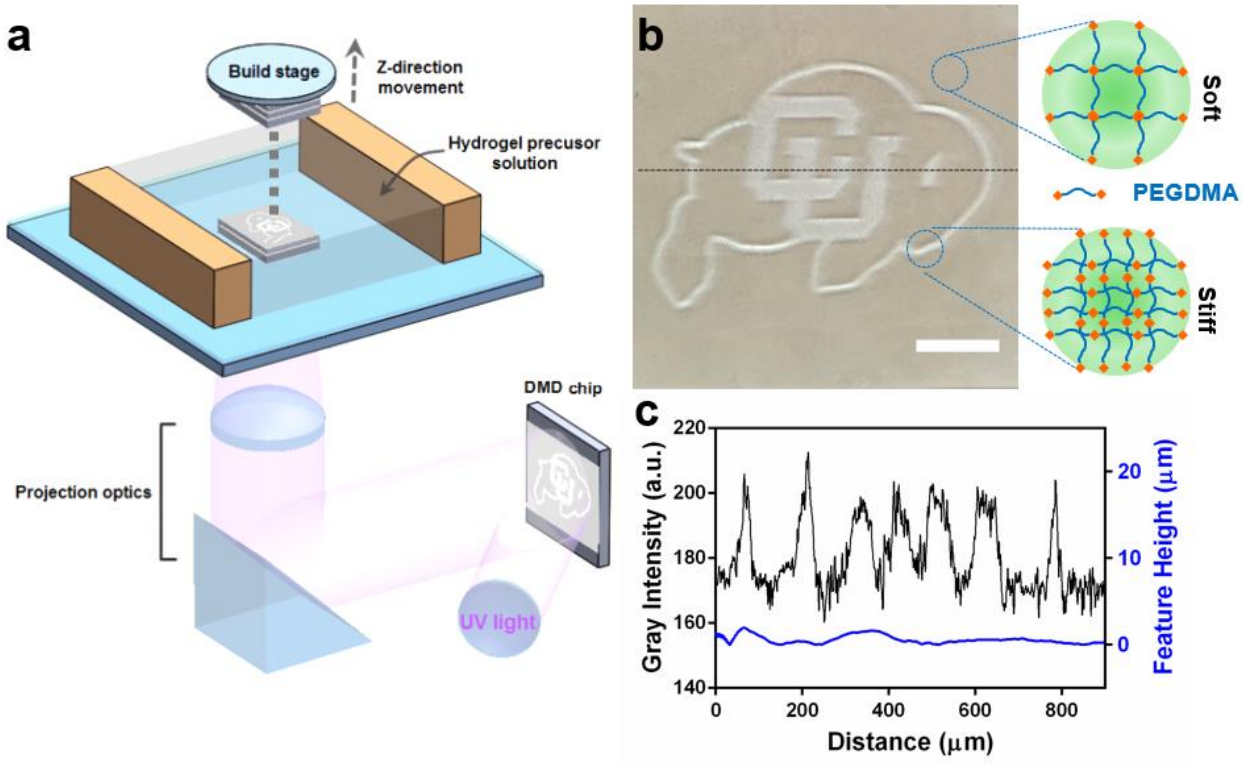

Figure 5.1 (a) Schematic of the lithography process. (b) Digital image of the fabricated hydrogel with different stiffness. Scale bar, 200 μm. (c) Optical contrast profile and surface roughness profile of the dot line.

5.3 3D Stiffness and topography characterization

Nano indentation of AFM has emerged as a useful tool to test the elastic modulus for biological samples. Various models have been developed to calculate moduli, but most of them are based on the Hertz model [2, 3]. In the Hertz model, it is assumed that the sample is an isotropic and linear elastic solid occupying an infinitely extending space. Furthermore, the interactions between indenter and sample are neglected, and the indenter is not deformable. Under these assumptions, the Young's modulus of the sample can be fitted using the Hertz model:

$$E = \frac{3(1-v^2)F}{4R^{\frac{1}{2}}\delta^{\frac{3}{2}}}$$

where $F = k_c * d$, k_c is the spring constant of the cantilever, R is the radius of the sphere tip, and $\delta = \Delta z - \Delta d$ is the indentation. Poisson's ratio is usually set to 0.4 [3].

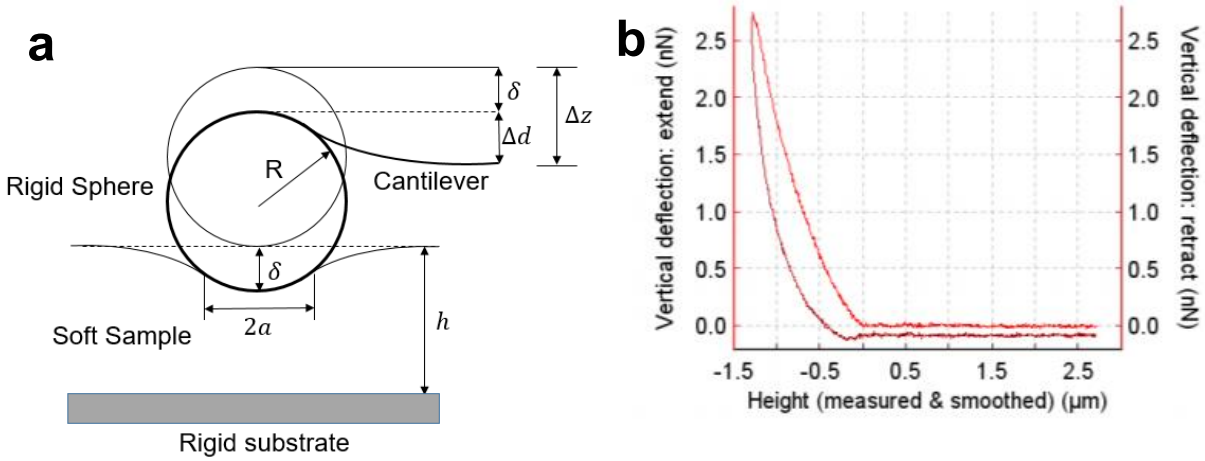

Figure 5.2 (a) Schematic of the indentation of AFM tip. (b) Example of an extend and retract curve [2].

The formula used with sphere indenters is shown in figure 5.2(a), while other indenters with different shapes can also be used to fit different scale of measurements. Usually, the materials for indentation tests have neither homogeneity nor should they be regarded as having absolute

elastic behavior. An example of the extend and retract in figure. 5.2(b) shows there is a hysteresis. The viscous relaxation of the material is one explanation for this phenomenon. And the higher rate of the loading, the smaller the indentation because there will be a larger resistant force coming from the viscose part of the material. However, if the indentation rate is too small, it can cause irreversible reorganization of the sample, so an appropriate speed should be applied.

Figures 5.3 (A) and (B) are two examples of fitted results of the Hertz model with and without bleomycin-treated mouse lung parenchyma. AFM is a valuable method to test the stiffness for engineered biomaterials or tissues with high resolution.

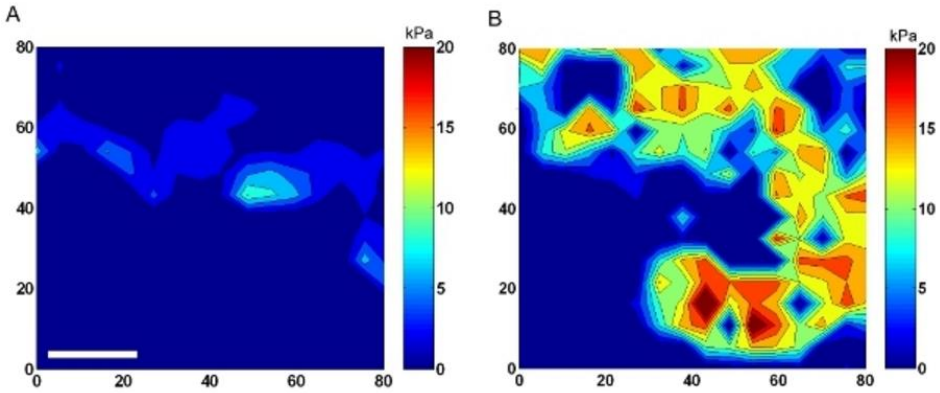

Figure 5.3 (A) and bleomycin-treated (B) mouse lung parenchyma. The color bars indicate shear modulus in kilopascals. Axis labels indicate spatial scale in micrometers. Scale bar: 20 μm [3]

In order to fabricate 3D structures with controlled stiffness, multi-layer hydrogels have been made. Figure 5.4(a) is the top view of a 6-layer structure with each layer having the same grayscale pattern, in which the middle line was exposed with 15 $\mathrm{mW/cm^2}$ and the background was 5 $\mathrm{mW/cm^2}$. After one layer was fabricated, the building stage moved up to practice layer-by-layer printing. For this structure, the layer height was set to be 70 μm. To characterize the 3D structure stiffness, AFM measurement based on the Hertz model was used. The 3D printed structure was soaked into PBS solution which allows the hydrogel to absorb water until it reaches an equilibrium status. And AFM measurements were done in the PBS solution as well to prevent

the hydrogel from drying out during the test. Figure 5.4(b) shows the results of an elasticity test of AFM. In the middle, the red line has the modulus around 10 kPa while the background was around 5 kPa. This proves that higher dosages can cause further crosslinking of the hydrogel and make the local area stiffer. It was necessary to show the difference in dosage contributed no difference to the surface topography as well. Figure 5.4(c) is the map of the contact point of AFM tip with the sample, which was recorded from the same points used to measure modulus in figure 5.4(b). It was clearly shown that the range of topography difference is within 600 nm.

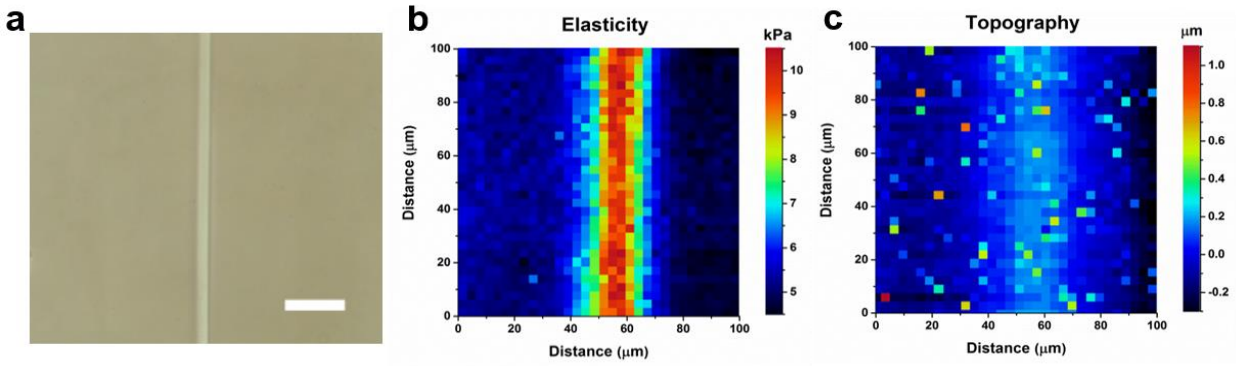

Figure 5.4 (a) Digital image of the top view of a multilayer structure. Scale bar, 100 μm. (b) AFM Young's modulus image. (c) AFM contact point image.

To get a better understanding of the relation between stiffness and power intensity, quantitative measurement was done. The test pattern was designed to be 8 300 by 300 μm^2 squares but with different power density from 5 mW/cm^2 to 15 mW/cm^2. A 3D structure was made by repeating the exposure and lifting the same 2D pattern for 6 layers, and each layer was 70 μm high. After the fabrication, elasticity test was practiced on 8 different squares with 3 different areas and the test for the height of each pad was done with profilometer. Figure 5.5 shows the result of the modulus and the height, where an obvious increase in the modulus can be observed while the

structure height remained nearly the same at 400 μm high. While keeping the structure at the same height, a range of ~2 kPa to ~16 kPa stiffness can be obtained with fine control over the grayscale.

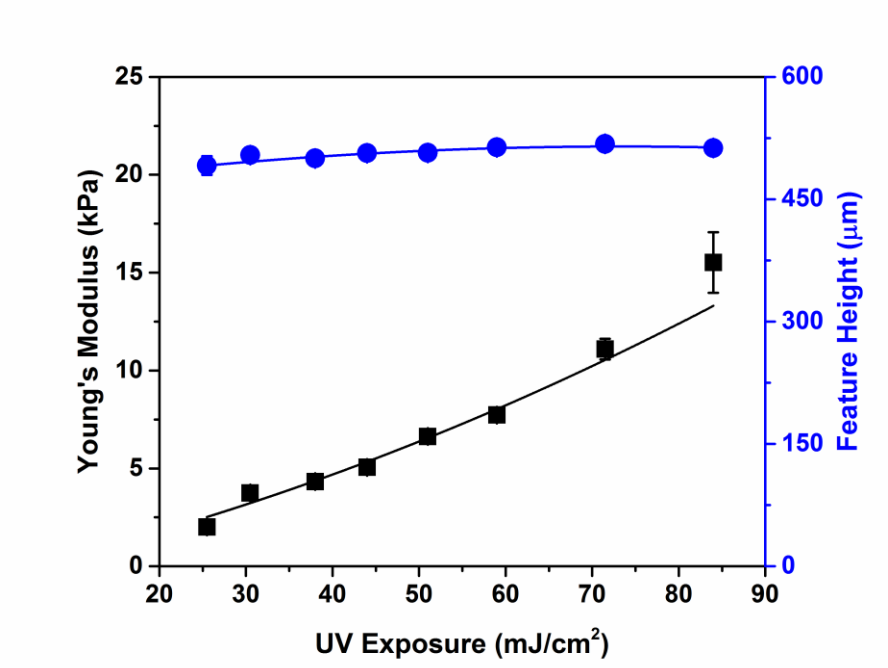

Figure 5.5 Modulus and height with various power density exposure.

5.4 Qualitative 3D stiffness demonstration

To demonstrate the effect of stiffness on 3D structures, different structures were fabricated. In figure 5.6(a), 4 rods with same size (100 μm diameter) and same height (20 layers, each layer was 50 μm high) but different power densities were made. The two rods with relatively higher power density stand well with small bending angles. The rod with the second least power density bent at a bigger angle and collapsed onto the other rod. The rod with the lowest relative power intensity bent and fell. The higher the power density used during the printing, the greater the

crosslinking density the structure had. This is the reason why structures created with the same exposure time and with the same geometrical appearance will have different shapes. In another experiment, the same amount of load was printed at the top of two rods in order to illustrate how difference in power density affect the stiffness of structures. In figure 5.6(b), two rods were printed using the same power density (15 $\mathrm{mW/cm^2}$) and they stand straight without bending under the load. In figure 5.6(c), two rods with different power densities were made. The left one was 5 $\mathrm{mW/cm^2}$ and the right one was 15 $\mathrm{mW/cm^2}$. It can be observed that the load tilted to the left rod which is the softer one. In figure 5.6(d), both rods were printed with 5 $\mathrm{mW/cm^2}$ and because the rods are both soft they could not bear the load and collapsed.

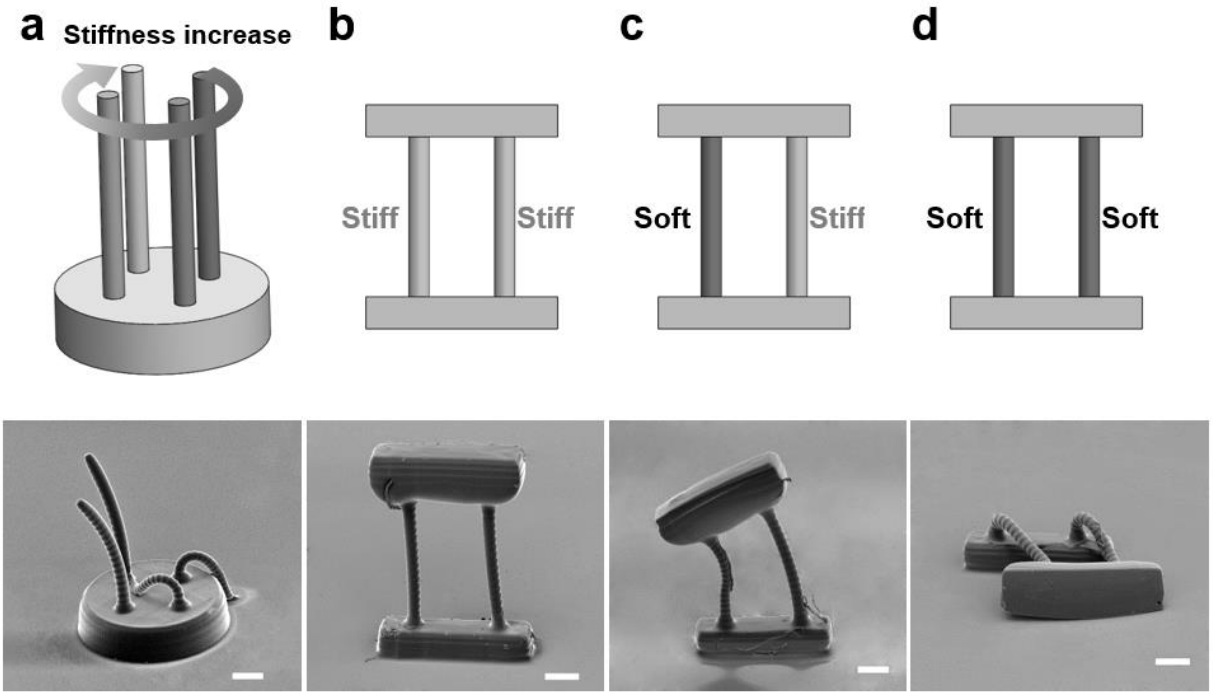

Figure 5.6 (a) Four rods with various power density. Scale bar, 200 μm. (b) Load on two stiff rods. Scale bar, 200 μm. (c) Load on one stiff and one soft rod. Scale bar, 200 μm. (d) Load on two soft rods. Scale bar, 200 μm.

5.5 Effect of stiffness on cellular behavior

To demonstrate the ability of programmed elasticity to direct cell behavior, a 2D elasticity patterns with alternate soft and stiff line structures (line width ~100 μm) was printed across a bulk hydrogels (Figure 5.7a). After surface functionalization of the patterned hydrogels with ECM protein fibronectin via Sulfo-SANPAH crosslinker, bovine pulmonary artery smooth muscle cells (bPASMCs) were then seeded and cultured on patterned hydrogels. Cells adhered preferentially to regions of stiff lines, replicating the pattern shape with high fidelity (Figure 5.7b), agreeing with previous studies of cell attachment to stiff regions on 2D patterned hydrogels [18, 19, 53]. Quantification of cell density further confirmed the observed differences in cell attachment (Figure 5.7c). For the limited number of cells attached on regions of soft lines, the cell aspect ratio (measure of cell elongation, Figure 5.7d) and cell alignment (relative to matrix line pattern, Figure 5.7e) was drastically different from regions of stiff lines. Cells attached on regions of stiff lines were considerably more elongated and perfectly aligned along patterned lines compared to regions of soft lines.

In addition to spatial guidance of cell attachment and morphology on 2D elasticity patterns, we then explored, whether cell behavior can be specifically directed in 3D hydrogel structures with spatially programmed elasticity. Therefore, a vascular tube structure with either uniform stiff wall or soft/stiff (0.5/0.5) wall was printed (Figure 5.7f, g). When the bPASMCs were seeded in high density on these vascular tubes which were covalently attached on treated cover glass, cells formed a monolayer around the tubes on cover glass and then start to migrate up to the wall of tubes in 3-days culture. For stiff tube, cells migrated up to the entire wall and formed 3D cell layers surrounding the outer and inner walls of the tube, which could predict 3D vascular tube formation *in vitro* (upper panels in Figure 5.7h, i). For soft/stiff tube, intriguingly, cells were almost

exclusively migrated up to stiff regions of wall, inducing a 3D half vascular tube formation (lower panels in Figure 5.7h, i). Directional cell migration is critical in many physiological and pathological processes, such as development, wound healing and angiogenesis, and has been well studied *in vitro* [8, 46]; however, directed cell migration in 3D structures is still challenging. Herein, by programming matrix elasticity in 3D microenvironments, our current platform provides not only feasibility to reconstruct organ-level vascular functions but also prominent tool for directional cell locomotion in 3D structures, which is promising for broad applications in tissue engineering and regenerative medicine.

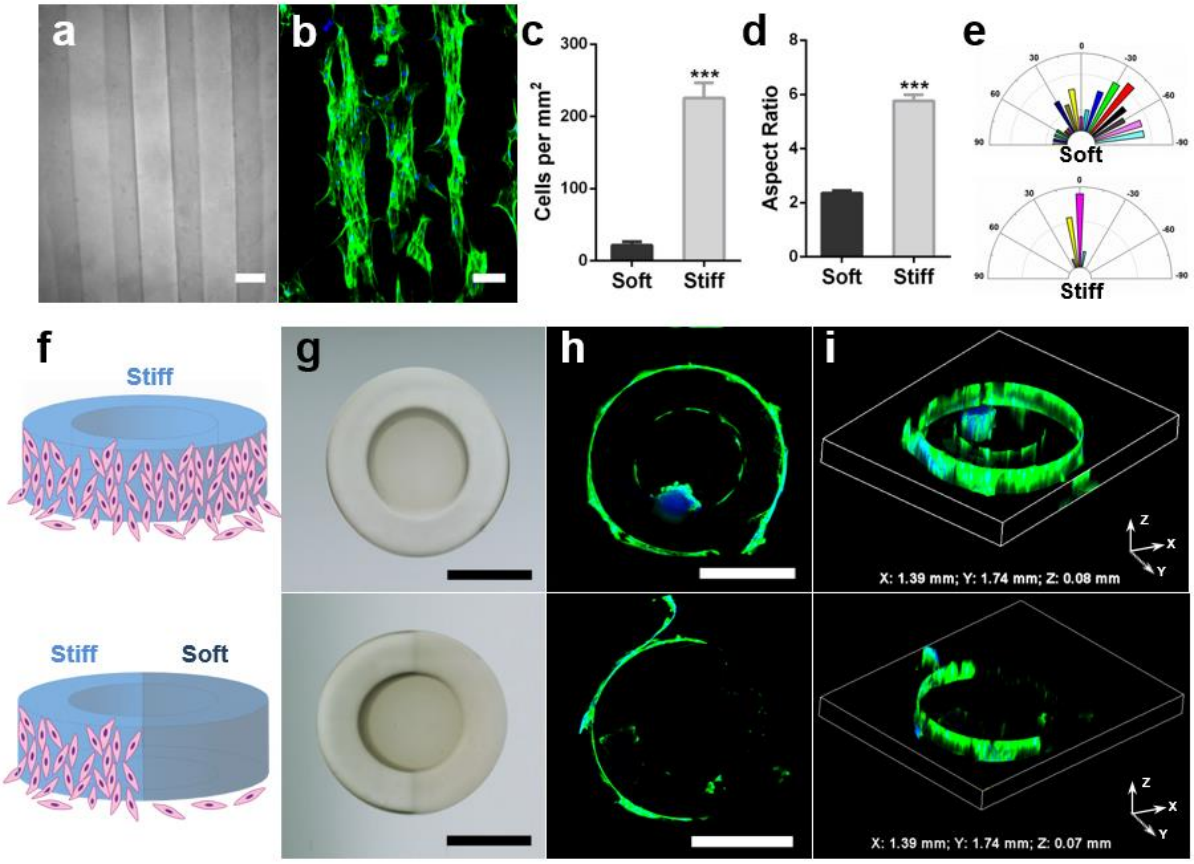

Figure 5.7(a) Bright-field image of elasticity line pattern (soft: dark line; stiff: bright line; line width: 100 μm). (b) bPASMCs cultured on elasticity line pattern. Quantification of number of cells per mm^2 (c), aspect ratio (d), and alignment (0 degree being perfectly aligned to the pattern) (e). (f) Schematics of micro-tube structure with all stiff and soft/stiff regions. (g) Bright-field images of stiff and soft/stiff micro-tube structures. Confocal X-Y projection (h) and 3D view (i) show bPASMCs cultured on micro-tube structure prefer to migrate up to stiff wall versus soft wall, and form the vascular smooth muscle tube structure. Green: f-actin. Blue: nuclei. Scale bars are: (a), (b) 100 μm; (g), (h) 500 μm.

5.6 Cell culture method

Cell Culture: Primary bovine pulmonary arterial smooth muscle cells (bPASMCs) were isolated from distal bovine vascular arteries as described previously [54], and cultured in DMEM (15-018-CV, Corning) supplemented with 10% bovine calf serum (BCS; 100-506, GemCell), 4 mM L-glutamine, 100 IU/mL penicillin, 100 μg/mL streptomycin, and 1% non-essential amino acid in an incubator at 37°C and 5% CO_2. Cells at passages of 3–5 were used for all the experiments.

Prior to cell seeding, the printed hydrogel structures were immersed in sterile PBS at 37 °C, and washed three times daily for 2 days to remove any unreacted PEGDMA monomers, free radicals and UV absorbers. Following that, the surface of printed hydrogel structures were activated with sulfo-SANPAH and subsequently functionalized with fibronectin as previously described [55]. Briefly, hydrogel structures were treated twice with sulfo-SANPAH (1 mg/mL in DI water; ProteoChem, Denver, CO) under UV light (5 mW cm^{-2}) for 15 min. The hydrogels were washed by sterile PBS thrice, followed immediately by incubation with human plasma fibronetin (0.1 mg/mL in PBS; EMD Millipore, Billerica, MA) overnight at 4 °C.

bPASMCs were seeded at a density of 1×10^4 (for 2D patterned line structures) or 2.5×10^4 (for 3D patterned tube structures) cells cm^{-2} at serum free media, rinsed with PBS after 2 h incubation at 37 °C, and cultured for 3 days in growth media with 10% BCS (refreshed on day 2). Cells were fixed in 4% formalin for 15 min, permeabilized with 0.1% Triton X-100 for 15 min, stained for F-actin (FITC-phalloidin, Life Technologies) and nuclei (DAPI, Life Technologies) for 45 min, and imaged by Spinning Disc confocal microscopy. Cell counts per mm^2 were measured by thresholding images of nuclei (10× magnification) in ImageJ and analyzing the number of nuclei via the built in function in ImageJ (eight distinct images per region of interest: soft and stiff). Cell aspect ratio, i.e. major axis / minor axis of the cells, and cell alignment angle, i.e. the angle

between major axis of cells and axis of line pattern, were manually measured in ImageJ (10× magnification, > 100 cells per region of interest).

Statistical Analysis: Statistical differences between compared groups were determined using unpaired t-tests with a *p*-value less than 0.05 indicating significance.

Chapter 6 Summary

In this thesis, a projection stereolithography system was developed, including the design and development of the optical system, motion control and printing process. A model of free radical polymerization was utilized to simulate the photopolymerization of materials used in these experiments during printing. The system was characterized and tested, and several structures were printed to show its 3D printing capabilities. Next, a fabrication process for 3D hydrogel structures with stiffness control based on a grayscale printing method was illustrated, and the stiffness provided by various exposure dosages were measured using AFM and Hertz model assumptions. The qualitative phenomenon of buckling standing rods was also shown as a visual explanation of the effect of crosslinking density on 3D structures. Finally, bovine pulmonary arterial smooth muscle cells were seeded on various structures and some interesting results were observed, including the cells' preference for staying on stiff regions and their migration to stiff regions.

Future work to improve the technology and expand its applications can include the elimination of the anisotropy in the areas where layers connect and the incorporation of shape memory polymers as printing materials. Methods to address the former may be to lower the power intensity along the edges of the images while still using the grayscale method [56], or to continuously lift the structure from the liquid interface [29] as opposed to moving in steps. Shape memory materials would be an exciting advancement as they could serve as actuators responding to different stimuli, and they have already been used in 3D printing. This thesis, along with the many studies in this area, broadens the potential beneficial applications of 3D printing.

Bibliography

[1] Lee B. Introduction to digital micromirror device (DMD) technology. Application Report of Texas Instruments 2013.

[2] Neumann T. Determining the elastic modulus of biological samples using atomic force microscopy. JPK Instruments Application Report 2008:1-9.

[3] Liu F, Tschumperlin DJ. Micro-mechanical characterization of lung tissue using atomic force microscopy. JoVE (Journal of Visualized Experiments) 2011:e2911-e.

[4] Murphy SV, Atala A. 3D bioprinting of tissues and organs. Nature biotechnology 2014;32:773-85.

[5] Thoma CR, Zimmermann M, Agarkova I, Kelm JM, Krek W. 3D cell culture systems modeling tumor growth determinants in cancer target discovery. Advanced drug delivery reviews 2014;69:29-41.

[6] Puschmann TB, Zandén C, De Pablo Y, Kirchhoff F, Pekna M, Liu J, et al. Bioactive 3D cell culture system minimizes cellular stress and maintains the in vivo-like morphological complexity of astroglial cells. Glia 2013;61:432-40.

[7] Hadjipanayi E, Mudera V, Brown R. Close dependence of fibroblast proliferation on collagen scaffold matrix stiffness. Journal of tissue engineering and regenerative medicine 2009;3:77.

[8] Lo C-M, Wang H-B, Dembo M, Wang Y-l. Cell movement is guided by the rigidity of the substrate. Biophysical journal 2000;79:144-52.

[9] Bershadsky AD, Balaban NQ, Geiger B. Adhesion-dependent cell mechanosensitivity. Annual review of cell and developmental biology 2003;19:677-95.

[10] Ouyang L, Highley CB, Sun W, Burdick JA. A Generalizable Strategy for the 3D Bioprinting of Hydrogels from Nonviscous Photo-crosslinkable Inks. Advanced Materials 2016.

[11] Mannoor MS, Jiang Z, James T, Kong YL, Malatesta KA, Soboyejo WO, et al. 3D printed bionic ears. Nano letters 2013;13:2634.

[12] Muth JT, Dixon PG, Woish L, Gibson LJ, Lewis JA. Architected cellular ceramics with tailored stiffness via direct foam writing. Proceedings of the National Academy of Sciences 2017:201616769.

[13] Sun C, Fang N, Wu D, Zhang X. Projection micro-stereolithography using digital micro-mirror dynamic mask. Sensors and Actuators A: Physical 2005;121:113-20.

[14] Manias E, Chen J, Fang N, Zhang X. Polymeric micromechanical components with tunable stiffness. Applied Physics Letters 2001;79:1700-2.

[15] Lu Y, Mapili G, Suhali G, Chen S, Roy K. A digital micro-mirror device-based system for the microfabrication of complex, spatially patterned tissue engineering scaffolds. Journal of Biomedical Materials Research Part A 2006;77:396-405.

[16] Xia C, Fang N. Fully three-dimensional microfabrication with a grayscale polymeric self-sacrificial structure. Journal of Micromechanics and Microengineering 2009;19:115029.

[17] Zhu W, Li J, Leong YJ, Rozen I, Qu X, Dong R, et al. 3D-Printed Artificial Microfish. Advanced materials 2015;27:4411-7.

[18] Norris SC, Tseng P, Kasko AM. Direct Gradient Photolithography of Photodegradable Hydrogels with Patterned Stiffness Control with Submicrometer Resolution. ACS Biomaterials Science & Engineering 2016;2:1309-18.

[19] Hribar KC, Choi YS, Ondeck M, Engler AJ, Chen S. Digital Plasmonic Patterning for Localized Tuning of Hydrogel Stiffness. Advanced functional materials 2014;24:4922-6.

[20] Kloxin AM, Kasko AM, Salinas CN, Anseth KS. Photodegradable hydrogels for dynamic tuning of physical and chemical properties. Science 2009;324:59-63.

[21] Caliari SR, Vega SL, Kwon M, Soulas EM, Burdick JA. Dimensionality and spreading influence MSC YAP/TAZ signaling in hydrogel environments. Biomaterials 2016;103:314-23.

[22] Ikuta K, Hirowatari K. Real three dimensional micro fabrication using stereo lithography and metal molding. Micro Electro Mechanical Systems, 1993, MEMS'93, Proceedings An Investigation of Micro Structures, Sensors, Actuators, Machines and Systems IEEE: IEEE; 1993. p. 42-7.

[23] Bertsch A, Zissi S, Jezequel J, Corbel S, Andre J. Microstereophotolithography using a liquid crystal display as dynamic mask-generator. Microsystem technologies 1997;3:42-7.

[24] Zhang X, Jiang X, Sun C. Micro-stereolithography of polymeric and ceramic microstructures. Sensors and Actuators A: Physical 1999;77:149-56.

[25] Gou M, Qu X, Zhu W, Xiang M, Yang J, Zhang K, et al. Bio-inspired detoxification using 3D-printed hydrogel nanocomposites. Nature communications 2014;5.

[26] Pyo S-H, Wang P, Zhu W, Hwang H, Warner JJ, Chen S. Continuous Optical 3D Printing of Green Aliphatic Polyurethanes. ACS Applied Materials & Interfaces 2016.

[27] Zhu W, Qu X, Zhu J, Ma X, Patel S, Liu J, et al. Direct 3D bioprinting of prevascularized tissue constructs with complex microarchitecture. Biomaterials 2017;124:106-15.

[28] Song X, Chen Y, Lee TW, Wu S, Cheng L. Ceramic fabrication using mask-image-projection-based stereolithography integrated with tape-casting. Journal of Manufacturing Processes 2015;20:456-64.

[29] Tumbleston JR, Shirvanyants D, Ermoshkin N, Janusziewicz R, Johnson AR, Kelly D, et al. Continuous liquid interface production of 3D objects. Science 2015;347:1349-52.

[30] Chia HN, Wu BM. Recent advances in 3D printing of biomaterials. Journal of biological engineering 2015;9:4.

[31] O'Brien AK, Bowman CN. Impact of oxygen on photopolymerization kinetics and polymer structure. Macromolecules 2006;39:2501-6.

[32] Dendukuri D, Pregibon DC, Collins J, Hatton TA, Doyle PS. Continuous-flow lithography for high-throughput microparticle synthesis. Nature materials 2006;5:365-9.

[33] Bryant SJ, Nuttelman CR, Anseth KS. Cytocompatibility of UV and visible light photoinitiating systems on cultured NIH/3T3 fibroblasts in vitro. Journal of Biomaterials Science, Polymer Edition 2000;11:439-57.

[34] Williams CG, Malik AN, Kim TK, Manson PN, Elisseeff JH. Variable cytocompatibility of six cell lines with photoinitiators used for polymerizing hydrogels and cell encapsulation. Biomaterials 2005;26:1211-8.

[35] Fedorovich NE, Oudshoorn MH, van Geemen D, Hennink WE, Alblas J, Dhert WJ. The effect of photopolymerization on stem cells embedded in hydrogels. Biomaterials 2009;30:344-53.

[36] Fairbanks BD, Schwartz MP, Bowman CN, Anseth KS. Photoinitiated polymerization of PEG-diacrylate with lithium phenyl-2, 4, 6-trimethylbenzoylphosphinate: polymerization rate and cytocompatibility. Biomaterials 2009;30:6702-7.

[37] O'Brien AK. The Impact of Oxygen on Photopolymerization Kinetics
and Polymer Structure: University of Colorado; 2005.

[38] Kızılel S, Pérez - Luna VH, Teymour F. Mathematical model for Surface - Initiated photopolymerization of poly (ethylene glycol) diacrylate. Macromolecular theory and simulations 2006;15:686-700.

[39] Decker C, Jenkins AD. Kinetic approach of oxygen inhibition in ultraviolet-and laser-induced polymerizations. Macromolecules 1985;18:1241-4.

[40] Lin H, Freeman BD. Gas permeation and diffusion in cross-linked poly (ethylene glycol diacrylate). Macromolecules 2006;39:3568-80.

[41] Neumann MG, Miranda WG, Schmitt CC, Rueggeberg FA, Correa IC. Molar extinction coefficients and the photon absorption efficiency of dental photoinitiators and light curing units. Journal of dentistry 2005;33:525-32.

[42] Wypych G. Handbook of UV degradation and stabilization: ChemTec PublishingElsevier Science & Technology Books [Distributor]; 2015.

[43] Goodner MD, Bowman CN. Development of a comprehensive free radical photopolymerization model incorporating heat and mass transfer effects in thick films. Chemical Engineering Science 2002;57:887-900.

[44] Lecamp L, Lebaudy P, Youssef B, Bunel C. Influence of UV radiation wavelength on conversion and temperature distribution profiles within dimethacrylate thick material during photopolymerization. Polymer 2001;42:8541-7.

[45] Odian G. Reactions of polymers. Principles of Polymerization, Fourth Edition 1991:729-88.

[46] Isenberg BC, DiMilla PA, Walker M, Kim S, Wong JY. Vascular smooth muscle cell durotaxis depends on substrate stiffness gradient strength. Biophysical journal 2009;97:1313-22.

[47] Engler AJ, Griffin MA, Sen S, Bönnemann CG, Sweeney HL, Discher DE. Myotubes differentiate optimally on substrates with tissue-like stiffness. J Cell Biol 2004;166:877-87.

[48] Discher DE, Janmey P, Wang Y-l. Tissue cells feel and respond to the stiffness of their substrate. Science 2005;310:1139-43.

[49] Gunn JW, Turner SD, Mann BK. Adhesive and mechanical properties of hydrogels influence neurite extension. Journal of Biomedical Materials Research Part A 2005;72:91-7.

[50] Al-Nasassrah MA, Podczeck F, Newton JM. The effect of an increase in chain length on the mechanical properties of polyethylene glycols. European journal of pharmaceutics and biopharmaceutics 1998;46:31-8.

[51] Wong JY, Velasco A, Rajagopalan P, Pham Q. Directed movement of vascular smooth muscle cells on gradient-compliant hydrogels. Langmuir 2003;19:1908-13.

[52] Choi YS, Vincent LG, Lee AR, Kretchmer KC, Chirasatitsin S, Dobke MK, et al. The alignment and fusion assembly of adipose-derived stem cells on mechanically patterned matrices. Biomaterials 2012;33:6943-51.

[53] Lampi MC, Guvendiren M, Burdick JA, Reinhart-King CA. Photopatterned Hydrogels to Investigate Endothelial Cell Response to Matrix Stiffness Heterogeneity. ACS Biomaterials Science & Engineering 2017.

[54] Frid MG, Kale VA, Stenmark KR. Mature vascular endothelium can give rise to smooth muscle cells via endothelial-mesenchymal transdifferentiation. Circulation research 2002;90:1189-96.

[55] Fischer RS, Myers KA, Gardel ML, Waterman CM. Stiffness-controlled three-dimensional extracellular matrices for high-resolution imaging of cell behavior. Nature protocols 2012;7:2056-66.

[56] Pan Y, Zhao X, Zhou C, Chen Y. Smooth surface fabrication in mask projection based stereolithography. Journal of Manufacturing Processes 2012;14:460-70.